FRONTIERS OF PHYSICS

RESEARCH ARTICLE
Volume 18 / Issue 1 / 13301 / 2023

Energy band alignment of 2D/3D MoS_2/4H-SiC heterostructure modulated by multiple interfacial interactions

Huili Zhu[1], Zifan Hong[2], Changjie Zhou[1,†], Qihui Wu[3], Tongchang Zheng[1], Lan Yang[1], Shuqiong Lan[1], Weifeng Yang[2,‡]

1 Xiamen Key Laboratory of Ultra-Wide Bandgap Semiconductor Materials and Devices, Department of Physics, School of Science, Jimei University, Xiamen 361021, China
2 Department of Microelectronics and Integrated Circuit, School of Electronic Science and Engineering (National Model Microelectronics College), Xiamen University, Xiamen 361005, China
3 School of Marine Equipment and Mechanical Engineering, Jimei University, Xiamen 361021, China
Corresponding authors. E-mail: †zhoucj@jmu.edu.cn, ‡yangwf@xmu.edu.cn

Received July 15, 2022; accepted August 29, 2022

ABSTRACT

The interfacial properties of MoS_2/4H-SiC heterostructures were studied by combining first-principles calculations and X-ray photoelectron spectroscopy. Experimental (theoretical) valence band offsets (VBOs) increase from 1.49 (1.46) to 2.19 (2.36) eV with increasing MoS_2 monolayer (1L) up to 4 layers (4L). A strong interlayer interaction was revealed at 1L MoS_2/SiC interface. Fermi level pinning and totally surface passivation were realized for 4H-SiC (0001) surface. About 0.96e per unit cell transferring forms an electric field from SiC to MoS_2. Then, 1L MoS_2/SiC interface exhibits type I band alignment with the asymmetric conduction band offset (CBO) and VBO. For 2L and 4L MoS_2/SiC, Fermi level was just pinning at the lower MoS_2 1L. The interaction keeps weak vdW interaction between upper and lower MoS_2 layers. They exhibit the type II band alignments and the enlarged CBOs and VBOs, which is attributed to weak vdW interaction and strong interlayer orbital coupling in the multilayer MoS_2. High efficiency of charge separation will emerge due to the asymmetric band alignment and built-in electric field for all the MoS_2/SiC interfaces. The multiple interfacial interactions provide a new modulated perspective for the next-generation electronics and optoelectronics based on the 2D/3D semiconductors heterojunctions.

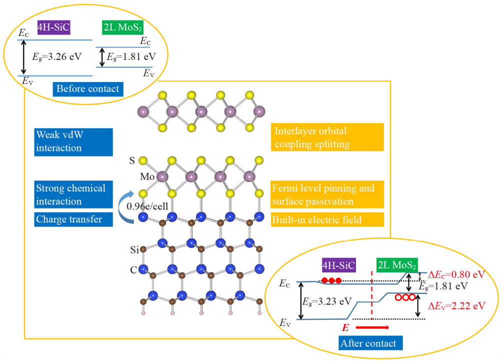

Keywords MoS_2, SiC, X-ray photoelectron spectroscopy, band alignment, first-principles calculations

1 Introduction

Low-dimensional materials with extraordinary peculiarities, such as zero-dimensional buckyballs and one-dimensional carbon nanotubes, have empowered their potentiality in many important fields [1, 2]. Their deficiency in distinguishing metal and semiconductor phases has led to the boomingly development of two-dimensional (2D) nanomaterials, including graphene, boron nitride, and transitional metal dichalcogenides (TMDCs), etc. [3–9]. In comparison with zero-bandgap graphene, layered TMDCs (MoS_2, WS_2, $MoSe_2$, WSe_2, etc.) exhibit a tunable bandgap of about 1–2 eV, showing an interesting capability for miniaturizing electronics. Among them,

https://doi.org/10.1007/s11467-022-1207-9

MoS_2 is the most optimistic TMDCs because of its surplus and innoxious and easily feasible synthesis [10, 11]. Structurally, MoS_2 is a typical hexagonal layered compound with strong in-plane covalent and weak out-of-plane van der Waals (vdW) interaction, resulting in the absence of dangling bonds on the surface [12]. When cleaved from bulk to monolayer (1L), energy band structure of MoS_2 transforms from indirect to direct due to the quantum confinement effect [6]. Field-effect transistors (FETs) based on monolayer MoS_2 have been demonstrated to exhibit a high on/off current ratio 10^8 and a high mobility of 200 $cm^2 \cdot V^{-1} \cdot s^{-1}$ at room temperature [13]. These intriguing properties give it a wide range of potential applications in transistors [13–15], memories [16, 17], flexible electronics [18, 19], photodetectors [20–23], energy storage and conversion and hydrogen evolution reaction [24].

In the past few decades, wide bandgap semiconductors (WBSs), such as GaN and SiC, have drawn considerable attention because of their outstanding properties, and widely used in the emerging electronics and optoelectronics. GaN possesses wide bandgap (3.4 eV), high room-temperature electron mobility (1300 $cm^2 \cdot V^{-1} \cdot s^{-1}$), and large short-wavelength absorption coefficient, making it an important semiconductor for applications in light emitting diodes (LED), FETs, solar cells, lasers, and photodetectors [25–29]. SiC exists as over 170 polytypes with the 4H polytype is most commonly used in high-temperature and high-frequency electronic devices due to its high carrier mobility (900 $cm^2 \cdot V^{-1} \cdot s^{-1}$), large band gap (3.26 eV) and low dopant ionization energy [30].

Beyond separate studies of 3D WBSs or 2D TMDCs, it is favourable to integrate 2D/3D TMDCs/WBSs heterostructures, which benefits for improving the performance of devices, such as LEDs, photodetectors, sensors and energy storage devices, and further providing the material platform of novel physical phenomena [25]. Due to the great light absorption of multilayer MoS_2, Goel et al. have successfully fabricated the MoS_2/GaN UV photodetector with the detectivity of 10^{11} Jones and the external spectral responsivity of 10^3 $A \cdot W^{-1}$ [31]. The MoS_2/GaN heterostructure device fabricated by Moun et al. demonstrated a detectivity of 10^{14} Jones and an ultra-high optical responsivity of 10^5 $A \cdot W^{-1}$ under a 405 nm laser radiation [32]. Because of its suitable band gap, SiC has always been an important material for UV photodetectors [33]. Then a MoS_2/4H-SiC photodetector operating in both the UV and visible regions were fabricated, which exhibits a responsivity of 5.7 $A \cdot W^{-1}$ under UV irradiation and a noise equivalent power (NEP) of 10^{-13}–10^{-15} $W \cdot Hz^{-1/2}$ [20]. Based on the dual-photogating effect, MoS_2/SiC photodetectors were demonstrated to have a ultra-high responsivity of 1.6×10^3 $A \cdot W^{-1}$ and 1×10^4 $A \cdot W^{-1}$ in VIS and UV irradiation, respectively [21]. The $MoSe_2$/WSe_2 heterojunction photodetector fabricated on n-doped 4H-SiC also shows the excellent performance with the maximum responsivity of 7.17 $A \cdot W^{-1}$, the corresponding maximum EQE of 1.67×10^3 %, and detectivity of 5.51×10^{11} Jones with a gain of 10^3 [34].

In the aspects of photocatalyst, gas sensor and other applications, the MoSSe/SiC and WSSe/SiC heterostructures were certified to be a high-efficient photocatalyst due to their specific electronic and optical properties based on the density functional theory (DFT) calculations [35]. And the MoS_2/GaN photoanode could enhance the photocurrent density to 5.2 $mA \cdot cm^{-2}$, which is 2.6 times higher than that of GaN photoanode [36]. As compared to the MoS_2 or GaN gas sensors, the sensitivity can be significantly enhanced (20 times) when integrating the MoS_2/GaN heterostructure [37, 38]. The MoS_2/GaN heterojunction nanowires could be used in memory device, which possesses the good retention characteristics of 3.4×10^3 s under a low switching voltage [39]. Although above experimental and theoretical works have confirmed the enormous advantage of the integrated TMDCs/WBSs, the detailed study and analysis of the interfacial properties, especially multiple interfacial interactions modulated energy band alignment, of these heterostructures are still quite limited.

In this study, monolayer (1L), bilayer (2L) and quadlayer (4L) MoS_2 were deposited on 4H-SiC (0001) substrates by reactive sputtering deposition. The interfacial properties of MoS_2/SiC heterostructures were studied by combining the first-principles calculations and X-ray photoelectron spectroscopy. Experimental (theoretical) VBO increases from 1.49 (1.46) to 2.19 (2.36) eV, with increasing MoS_2 layers up to 4L. Theoretical calculations further reveal that a strong interlayer interaction was demonstrated at 1L MoS_2/SiC interface and Fermi level pinning and totally surface passivation were realized for the 4H-SiC (0001) Si surface. 1L MoS_2/SiC interface exhibits type I band alignment with the asymmetric CBO and VBO. For 2L and 4L MoS_2/SiC, Fermi level was just pinning at the lower MoS_2 monolayer. They exhibit the type II band alignments and the enlarged CBOs and VBOs. High efficiency of charge separation will emerge due to the asymmetric band alignment and built-in electric field for all the MoS_2/SiC interfaces, and enhance the device performance significantly.

2 Experimental and theoretical methods

The 4H-SiC substrates were prepared using a four-step cleaning process. It was ultra-sonicated in acetone, ethanol and DI water for 10 mins each at 45 °C to remove particle and organic contaminants. After which, dilute HF (1:1) was used to etch the surface to remove any SiO_2 oxidation. MoS_2 layers were grown via reactive magnetron sputtering whereby a molybdenum target was sputtered using argon in a chamber with ambient sulfur. The partial pressure of sulfur vapour was controlled at 1.2 × 10^{-5} mbar through the heating of sulfur powder in a separate compartment. One of the substrates was left bare while the rest were sputtered with a DC power source at 10 W, 3.2 × 10^{-4} mbar and 700 °C for 5 mins, 9 mins, 12 mins and 2 hours (1L, 2L, 4L and bulk MoS_2).

Thermo Scientific DXR microscope with a 514.5 nm laser were used to take the Raman and photoluminescence (PL) spectra of the as-grown heterojunction samples. Atomic force microscopy (AFM) images were obtained by using the Bruker Dimension Icon system and the tapping mode. High-resolution transmission electron microscopy (TEM) images were taken from samples grown directly on 8 nm SiO_2 support membranes. High resolution X-ray photoelectron spectroscopy (XPS) spectra were taken on a VG ESCALAB 220i-XL XPS system. The binding energy scale was calibrated with pure Au, Ag, and Cu standard samples by setting the Au $4f_{7/2}$, Ag $3d_{5/2}$, and Cu $2p_{3/2}$ at binding energies of 83.98 eV, 368.26 eV, and 932.67 eV, respectively. C 1s signal from the sample surface was used to correct the core-level binding energy.

The first-principles calculations were performed by using the Vienna ab initio simulation package (VASP) [40]. The exchange-correlation energy is described by the Perdew-Burke-Ernzerhof (PBE) exchange-correlation functional [41]. The semi-empirical correction scheme of Grimme (DFT-D3) were utilized to correct the effect of vdW interactions in multilayer TMDCs system [42]. Furthermore, Heyd–Scuseria–Ernzerhof (HSE06) was used to simulate all the density of states (DOSs), because of its accuracy for obtaining the bandgap of the calculated system [43]. We also considered the dipole correction in the calculation to eliminate possible artificial dipole interactions [44]. The charge transfer was calculated by using the Bader analysis [45].

3 Results and discussion

Based on the above sputtering parameters, we could obtain the extremely low growth rate of MoS_2 layers. The successful deposition of monolayer and few-layer MoS_2 on different substrates have been achieved by precisely controlling the growing time, which has also been demonstrated by our previous works [46–50]. Raman spectroscopy was further used to characterize the number of layers in our samples. It has been shown in previous studies that the difference in Raman shift between the in-plane (E^1_{2g}) and out-of-plane (A_{1g}) characteristic vibration modes increases with the number of layers of MoS_2 and hence can be used to accurately determine the number of layers within 1 to 5 MoS_2 layers [51–53]. Figure 1(a) shows the E^1_{2g} and A_{1g} vibration modes of 1L, 2L, 4L and bulk MoS_2/SiC samples. A Raman shift difference of 19.5, 21.7, 23.9 and 25.5 cm^{-1} was observed from the samples, which corresponds to 1L, 2L, 4L and bulk MoS_2 respectively.

AFM images of SiC substrate before etching, after etching, and 1L MoS_2 grown on SiC substrate were

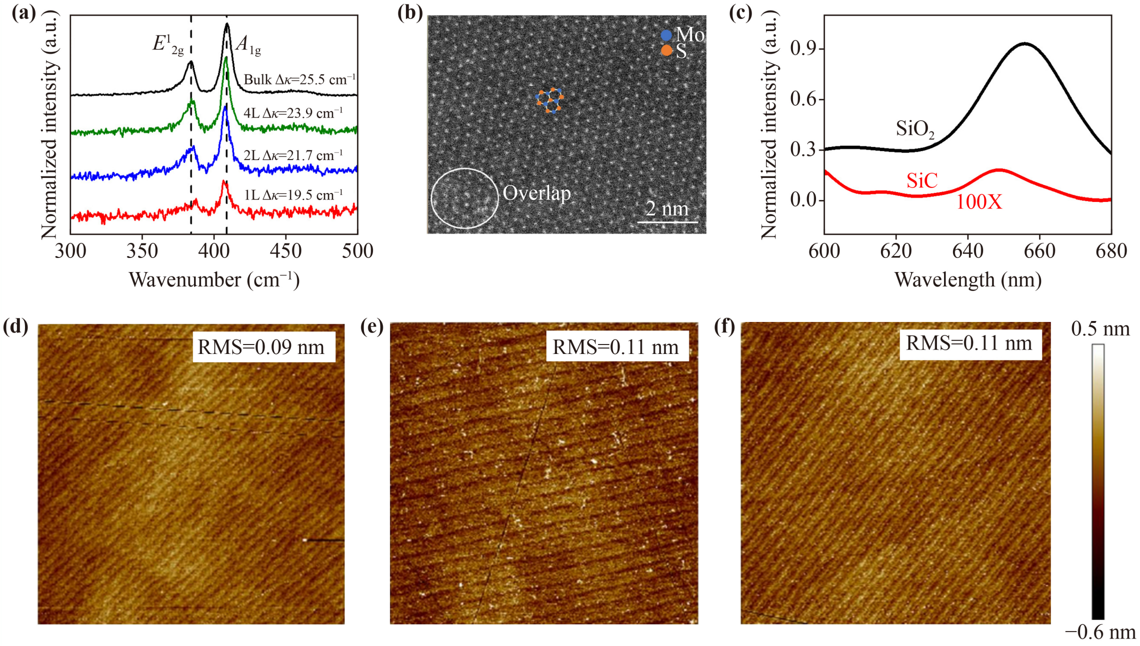

Fig. 1 **(a)** Raman spectra of 1L, 2L, 4L and bulk MoS_2/SiC, **(b)** ADF-STEM image of 1L MoS_2, **(c)** PL spectra of 1L MoS_2 grown on SiC against 100 nm SiO_2/Si. AFM images (5 μm × 5 μm) of **(d)** SiC substrate before etching, **(e)** SiC substrate after etching, **(f)** 1L MoS_2 grown on SiC substrate.

taken to determine the uniformity of the samples, as shown in Figs. 1(d)–(f). The step-terrace structure on the surface is due to different etching rates of the atomic layers in the 4H-SiC crystal structure during the material processing [54]. The dilute HF wet etching process only resulted in a slight increase in RMS value from 0.09 nm to 0.11 nm and the deposition of MoS_2 did not result in an increase in surface roughness showing good monolayer uniformity.

Figure 1(b) exhibits annular dark field STEM (ADF-STEM) image of monolayer MoS_2 with alternating Mo and S columns arranging into hexagonal structure, which can be identified to be the 2H-MoS_2 polytype. Meanwhile, moiré patterns (overlap on the lower left) are also observed. Therefore, TEM results confirm the high quality 2D MoS_2. Figure 1(c) shows the PL spectra of 1L MoS_2 grown on SiC and SiO_2 as a comparison. The PL intensity of the 1L MoS_2 on SiC was about 500× weaker in comparison to 1L MoS_2 grown on a 100 nm SiO_2/Si substrate. Though a tiny PL peaks were observed at 649 nm from the 1L MoS_2/SiC sample, the quenching of PL intensity forebodes a strong interaction between the as-grown MoS_2 and SiC substrate, which agrees well with the following theoretical observations. And no PL peaks were observed from 2L, 4L and bulk samples.

Surface chemistry was probed with XPS measurements. The fitting rule adopted in this work is that the full width at half maximum (FWHM) of both components are comparable and the intensity ratios follow the expect quantum mechanically predicted ratio when XPS doublet have narrow separations. Figure 2 shows the Si 2p scan for SiC, 1L, 2L and 4L MoS_2/SiC. The SiC Si 2p peak was resolvable into $2p_{1/2}$ and $2p_{3/2}$ peaks due to the asymmetry of the 2p peak and was done to enhance the accuracy of the subsequent band alignment calculations. The Si $2p_{3/2}$ peak for all samples except bulk MoS_2/SiC was aligned to the literature value of 100.4 eV to account for charging effects [55]. The spectra for the bare SiC showed no signs of atmospheric oxidation which supports that the etching process removed any surface oxidation on the SiC surface. A convoluted Si^{1+} peak can be observed at a binding energy of 102.07, 102.16 and 102.21 eV for the 1L, 2L and 4L MoS_2 grown samples. This is because the XPS characterization was done ex-situ and the MoS_2 grown samples were left in air for a longer time for deposition whereas the bare SiC substrate was characterized immediately after etching. Nonetheless, there was only a small amount of Si^{1+} present.

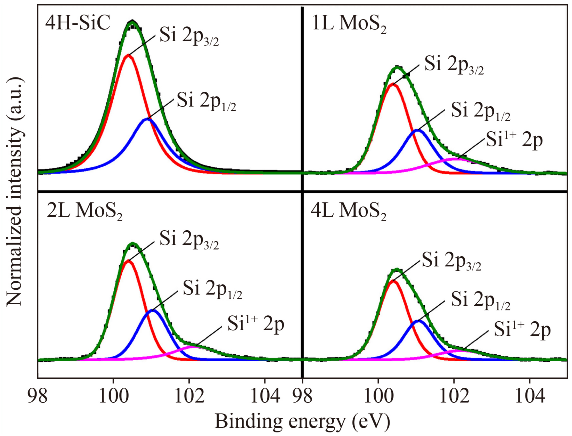

Fig. 2 XPS Si 2p spectra of SiC, 1L, 2L and 4L MoS_2/SiC.

Figure 3 shows the Mo 3d and S 2p scan for 1L, 2L, 4L and bulk MoS_2. The Mo^{4+} $3d_{5/2}$ and $3d_{3/2}$ peaks were located at 228.69, 228.59, 228.60 and 231.83, 231.78, 231.76 eV for 1L, 2L and 4L MoS_2/SiC. Whereas the S^{2-} $2p_{3/2}$ and $2p_{1/2}$ peaks were located at 161.50, 161.43, 161.42 and 162.69, 162.62, 162.62 eV respectively. This agrees well with the current literature values [56–59]. Due to the absence of the SiC peak in bulk MoS_2, the spectrum was aligned to the Mo $3d_{5/2}$ of 4L MoS_2 for presentation purposes. Due to incomplete sulfurization, small amounts of metallic Mo was detected on 2L (3.5 at %), 4L (3.0 at %) and bulk (2.0 at %) MoS_2.

To derive the band alignment of the MoS_2/SiC heterostructures, we adopted a direct method suggested by Santoni *et al.* [60], which requires to align the the XPS spectra of SiC, 1L, 2L and 4L MoS_2 to a common reference. The alignment has already been done to the Si $2p_{3/2}$ peak at 100.4 eV. The Si $2p_{3/2}$ peak in SiC was chosen to be the reference as it can be detected in all the required samples in sufficient quantity. The valence band maximum (VBM) was then derived by the intersection of the linear regressions of the leading edge of valence band and the baseline of its spectra, as shown in Fig. 4. The VBM of bare SiC was identified to be 1.26 eV. Interestingly, the valence band spectra of 1L, 2L and 4L MoS_2/SiC exhibit two leading edges with different slope. According the following theoretical density of states (DOS), the red linear regression of the leading edge comes from the Mo $4d_{z^2}$ orbital, while the

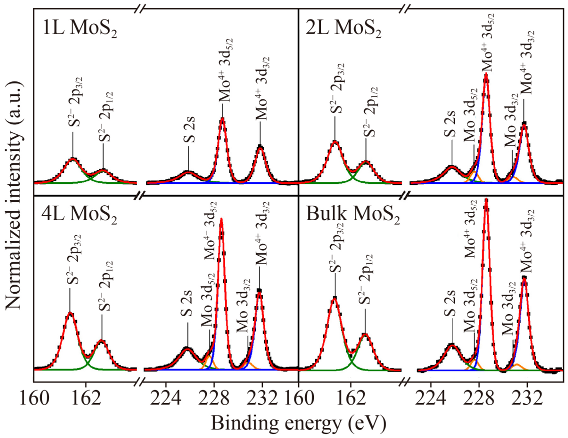

Fig. 3 XPS Mo 3d and S 2p spectra of 1L, 2L, 4L and bulk MoS_2/SiC.

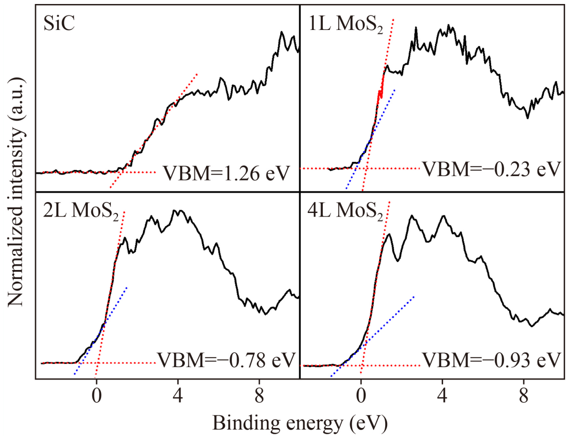

Fig. 4 Valence band spectra for SiC, 1L, 2L and 4L MoS$_2$/SiC.

blue one originates from the Mo 4d$_{(x^2-y^2)}$ orbital. It is the Mo 4d$_{(x^2-y^2)}$ orbital that contributes the VBM of 1L MoS$_2$. Then, the VBM of the 1L, 2L and 4L MoS$_2$/SiC could be identified to be –0.23, –0.78, and –0.93 eV, respectively. Further considering the VBM of SiC substrate of 1.26 eV, the valence band offsets (VBOs) could be obtained to be 1.49, 2.04, and 2.19 eV for the 1L, 2L and 4L MoS$_2$/SiC, respectively. Therefore, the VBOs increase from 1.49 eV up to 2.19 eV with increasing MoS$_2$ layers up to 4L.

To understand above experimental observations and illuminate the interfacial interactions and electronic properties in the MoS$_2$/4H-SiC heterostructures, the first-principles calculations were performed by using the Vienna ab initio simulation package (VASP). Figure 5 shows the optimized atomic structure of 1L MoS$_2$ and the HSE06 total DOSs of 1L MoS$_2$ and partial DOSs of Mo and S atom. The lattice constants of 3.19 Å and the HSE06 bandgap of 2.10 eV are obtained for 1L MoS$_2$. These basic parameters are in good agreement with the previous theoretical and experimental results [12, 61]. The conduction band minimum (CBM) and VBM mainly come from the Mo atom. Careful observation shows that the CBM mainly comes from the Mo 4d$_{z^2}$ orbital. The valence band mainly originates from the 4d$_{(x^2-y^2)}$ and 4d$_{z^2}$ orbitals, while it's the 4d$_{(x^2-y^2)}$ orbital that contributes the VBM of 1L MoS$_2$. The different orbital origins of the valence band lead to the formation of two different slope distributions in the DOS of MoS$_2$ at the valence band. This is consistent well with the above XPS valence band spectra of MoS$_2$, as exhibited in Fig. 4, and is beneficial to the accurate identification of the VBM of 1L, 2L and 4L MoS$_2$ in XPS valence bands.

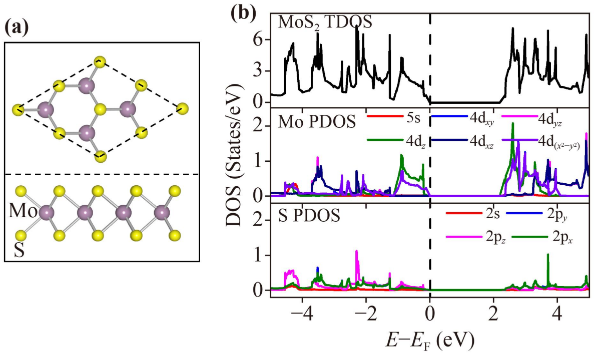

Fig. 5 **(a)** Top and side view of the optimized atomic structure of 1L MoS$_2$. **(b)** The HSE06 total DOSs of 1L MoS$_2$ and partial DOSs of Mo and S atom. The Fermi level is shifted to 0 eV.

The lattice constant of bulk 4H-SiC was obtained to be 3.09 Å, consistent with the reported value [62, 63]. The HSE06 bandgap is 3.49 eV, as shown in Fig. 6(b), which is only 7 % larger than the reported bandgap of 3.26 eV. The lattice constant of the substrate 4H-SiC was slightly expanded in the model constructed to make it consistent with the lattice constants of MoS$_2$, due to the weak vdW interlayer interaction in multilayer MoS$_2$, which will be constructed in our calculations. The bandgap of the strained bulk 4H-SiC is 3.10 eV, as shown in Fig. 6(b), which is only about 5 % smaller than the reported bandgap of 3.26 eV due to the slight tensile strain. Therefore, the model based on the strained 4H-SiC can effectively ensure the accurate results of the band alignment.

The 4H-SiC (0001) surface is usually formed by a Si or C atomic layer due to the polarity. Previous researches have demonstrated that the Si-face is energy stabilized surface as compared to the C-face [64]. Then

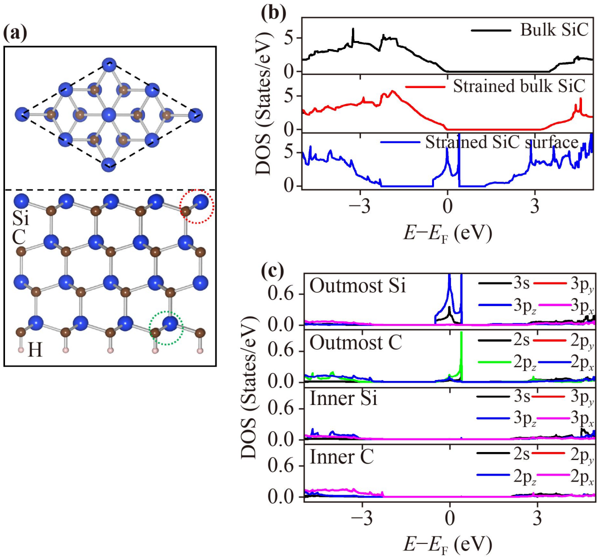

Fig. 6 **(a)** Top and side view of the strained atomic structure of 4H-SiC (0001) Si surface. **(b)** The HSE06 total DOSs of bulk, strained bulk 4H-SiC and strained 4H-SiC (0001) Si surface. **(c)** Partial DOSs of the outmost and inner Si and C atoms as indicated by the red and green circles in (a), respectively. The Fermi level is shifted to 0 eV.

the geometrical and electronic structures of 4H-SiC (0001) Si surface under slight tensile strain were adopted and calculated in this study. Figure 6(a) shows the strained atomic structure of 4H-SiC (0001) Si surface. Due to the Si dangling bond formed on the surface, the HSE06 total DOSs, as shown in Fig. 6(b), exhibit the strong surface states in the middle of the bandgap. And the Fermi level just passes through the surface states, indicating the Fermi level pinning, which is in agreement with the case of 2H-SiC (0001) Si surface [59]. Figure 6(c) shows the partial DOSs of the outmost and inner Si and C atoms as indicated by the red and green circles in Fig. 6(a), respectively. It is found that the mid-gap surface states mainly come from the outmost unsaturated Si atoms due to the broken Si-C bonds at the surface. It seems like that the outmost Si and C atomic layers contribute greatly to these surface states, while almost no surface states were observed in the bandgap for the inner Si and C atomic layers. Therefore, the inner Si and C atoms keep the electronic properties of bulk 4H-SiC.

Furthermore, 1L MoS_2/4H-SiC configuration was first constructed by a MoS_2 monolayer (containing 1 Mo, 2 S atomic layers) and 8 atomic layers of the 4H-SiC(0001) Si surface (containing 4 Si and 4 C atomic layers). Considering the lattice matching and hexagonal symmetry, six representational high-symmetric 1L MoS_2/4H-SiC configurations were constructed as shown in Figs. 7(a)–(f). The binding energies of these configurations were calculated by using the following equation:

$$E_b = E_{total} - E_{\mathrm{SiC}} - E_{\mathrm{MoS_2}}, \tag{1}$$

where E_{total}, E_{SiC} and $E_{\mathrm{MoS_2}}$ are the total energies of MoS_2/4H-SiC system, isolated 4H-SiC and MoS_2, respectively. Among above six possible configurations, the preferred atomic structure of 1L MoS_2/4H-SiC, as shown in Figs. 7(c) and (f), has the lowest binding energy of −0.96 eV. In this energy favorable configuration, S atom locates on the top of the Si atom of the 4H-SiC (0001) Si surface, while Mo atom is aligned with the C atom below. As shown in Fig. 7(f), a distinct Si-S chemical bond is formed at the 1L MoS_2/4H-SiC interface. Moreover, the Si-S bond length is calculated to be 2.20 Å. This value is shorter than the interlayer distance of 2.5–3.5 Å in the vdW systems and similar with the Si-S bond length of 2.0 Å in other covalent bonding system [65, 66]. Above large binding energy and formation of a chemical Si-S bond indicate a significantly strong interlayer interaction at the 1L MoS_2/4H-SiC interface, agreement well with the above experimental observation of the quenching of PL.

To identify the interface properties, especially the band alignment, atomic DOSs of 1L MoS_2/SiC interface were calculated and aligned from bottom to up according to the atomic order, as shown in Fig. 8(a). As compared to that of bare 4H-SiC (0001) Si surface, the original mid-gap surface states vanish when 1L MoS_2 layer adsorbed on the surface. That is, the surface states originated from the Si dangling bond was passivated by the S atom by forming the chemical Si-S bond. Though the absence of the dangling bond of the MoS_2 surface, the existing of lone pair at the S surface accounts for the surface passivation of the SiC substrate, according to our previous calculations [67]. Then the Fermi level shifts up and passes through the bottom of conductance band, indicating the Fermi level pinning at the interface states of the 1L MoS_2/4H-SiC interface.

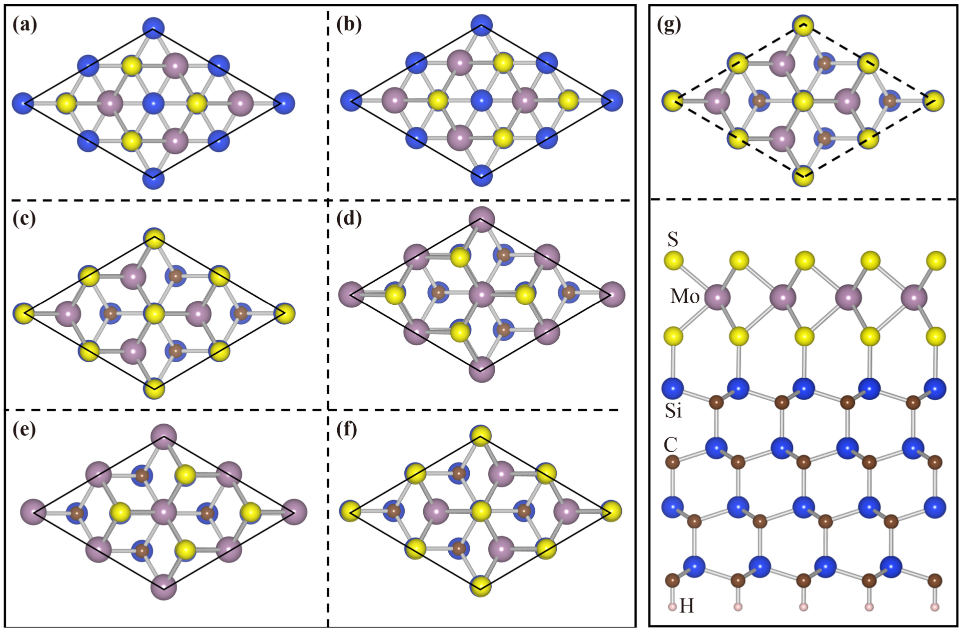

Fig. 7 **(a–f)** Top views of six representational high-symmetric 1L MoS_2/4H-SiC configurations. **(g)** Top and side view of the preferred atomic structure of 1L MoS_2/4H-SiC interface.

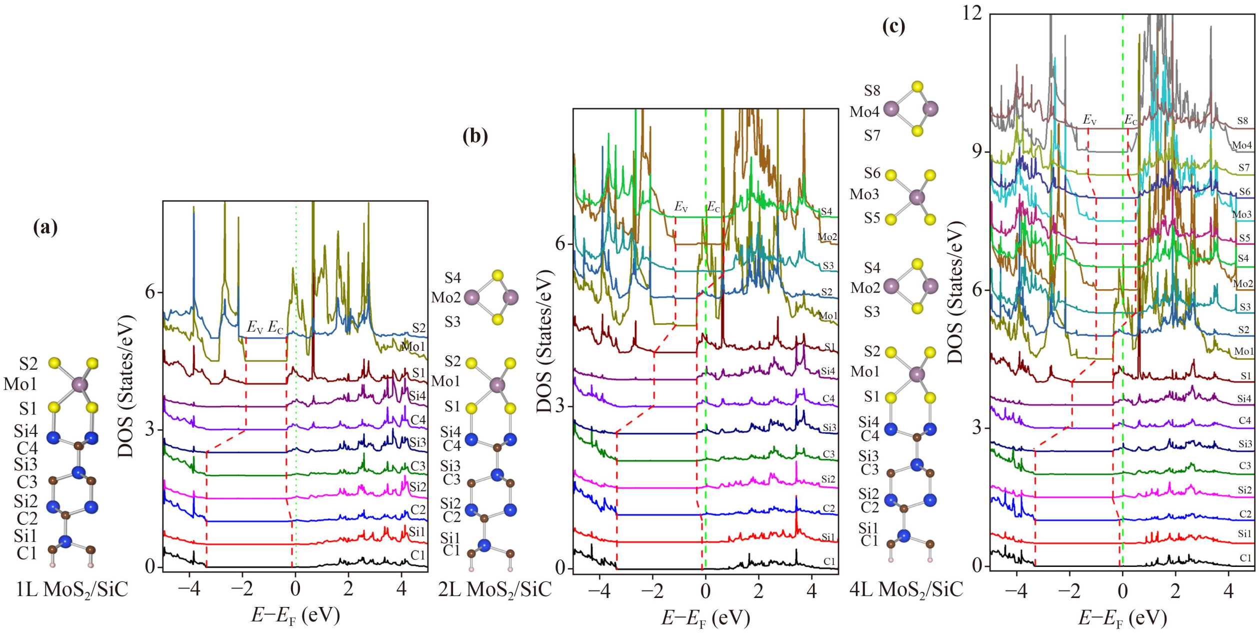

Fig. 8 **(a)** Atomic DOSs of 1L MoS$_2$/SiC, **(b)** 2L MoS$_2$/SiC, and **(c)** 4L MoS$_2$/SiC interfaces were calculated and aligned from bottom to up according to the atomic order illustrated in the left inset. The green dotted line indicates the Fermi level at 0 eV. The red dashed lines indicate the VBM and CBM of the different atomic layer of the MoS$_2$/SiC interface.

According to the real space atomic DOSs alignments, we could directly identify the VBM and CBM of each atomic layer and further obtained the band alignment at the 1L MoS$_2$/SiC interface, as indicated by the red dashed lines in Fig. 8. Atomic DOSs of bottom C1, Si1 and C2 exhibit the inner SiC electronic properties with the bandgap of about 3.23 eV. The CBM and VBM lie at the –0.13 and –3.36 eV, respectively. Looking up from Si2 to S2, the CBM shifts a little down to –0.33 eV. However, the VBM shifts largely up to –1.90 eV from C4 to S2. Then the bandgap shrinks from 3.23 eV to 3.03 eV, further to 1.57 eV from bottom to up in the 1L MoS$_2$/SiC heterostructure. And the CBM and VBM exhibits special asymmetric evolution, which would play important role in the carrier distribution. The new bandgap of 1L MoS$_2$ (1.57 eV) in 1L MoS$_2$/SiC heterostructure is much smaller than that of bare MoS$_2$ (2.10 eV), further indicating a strong interaction between MoS$_2$ and SiC. The interaction at the MoS$_2$/SiC interface is totally different from the previous weak interaction among the WS$_2$/HfO$_2$, MoS$_2$/HfO$_2$ and WS$_2$/SiO$_2$ interfaces [68–70]. The CBM and VBM distributions demonstrate the formation of type I band alignment at the 1L MoS$_2$/SiC interface. However, due to the special asymmetric evolution, the CBM locates at the SiC and MoS$_2$ region, while the VBM only lies at the MoS$_2$ region, different from the traditional type I band alignment.

Moreover, the charge transfer between 1L MoS$_2$ and SiC substrate was identified by using the Bader analysis [45]. The calculation results show that about 0.96e transfer from the SiC substrate to the MoS$_2$ layer. Since that, an electric field forms and it directs from SiC to MoS$_2$. The built-in electric filed is significantly important for the high performance of the electronic and optoelectronic devices based on the MoS$_2$/SiC heterostructure [20]. Combined with the built-in electric field and the special band alignment, the photogenerated holes tend to accumulate to the MoS$_2$ layer, while electrons tend to accumulate to the SiC layer. The efficiency of separation of photogenerated carriers is benefitting for enhancing the performance of the photodetectors and photocatalytic devices.

In order to understand the evolution of VBOs as the MoS$_2$ thickness increasing, atomic DOSs of 2L and 4L MoS$_2$/SiC interfaces were further calculated and aligned from bottom to up according to the atomic order, as shown in Figs. 8(b) and (c). According to our group's works by using the X-ray diffraction (XRD) and TEM [46, 47], the as-grown multilayer MoS$_2$ on different substrates tend to exhibits the 2H-phase. And our and others previous first-principles calculations [12, 71] also demonstrated that the 2H-phase MoS$_2$ generates the lowest formation energy in the multilayer stacking systems. Therefore, 2H-phase MoS$_2$ were mainly constructed to clarify the issue of band alignment evolution in this work. For 2L MoS$_2$/SiC interface, the Fermi level also passes through the interface states locating at the region between the lower MoS$_2$ monolayer and SiC substrate, similar with the case at 1L MoS$_2$/SiC interface. However for the upper MoS$_2$ layer, almost no interface states were observed in the bandgap and the Fermi level just passes through the center of the band gap. Therefore, Fermi level was just pinning at the interface states in the lower 1L MoS_2/SiC heterostructure. The interaction between the upper and lower MoS_2 layer keeps the weak vdW interaction. That is, the lower MoS_2 monolayer can effectively passivate the dangling bonds of the SiC surface and obtain a new weak vdW surface.

We could also identify the VBM and CBM of each atomic layer and obtain the band alignment at the 2L MoS_2/SiC interface, as indicated by the red dashed lines in Fig. 8(b). Similar with 1L MoS_2/SiC, atomic DOSs of bottom C1, Si1 and C2 also exhibit the inner SiC electronic properties with the bandgap of about 3.23 eV. The CBM and VBM also lie at the –0.13 and –3.36 eV, respectively. Looking up from Si2 to S2, the CBM firstly shifts a little down to –0.33 eV. Then, the CBM shifts largely up to 0.67 eV from S3 to S4, further indicating the weak vdW interaction between the upper and lower MoS_2 layer. For the VBM, it firstly shifts largely up to –1.95 eV from C4 to S1. Then, the VBM continues to shift up to –1.14 eV from Mo1 to S4 due to the interlayer orbital coupling interaction in bilayer MoS_2. The interlayer orbital coupling tends to split and shift the VBM to the higher energy region, which has been demonstrated in the previous theoretical calculations of multilayer MoS_2 [12]. Then the bandgap changes from 3.23 eV to 3.03 eV, 1.62 eV, 0.81 eV and 1.81 eV from bottom to up in the 2L MoS_2/SiC heterostructure. Therefore, the CBM and VBM exhibit more complicated asymmetric evolution, as compared with that of 1L MoS_2/SiC. The CBM locates at the interface from Si2 to S2, while the VBM locates at the MoS_2 layer from Mo1 to S4. On the whole, the complicated CBM and VBM evolution demonstrates the type II band alignment of the 2L MoS_2/SiC heterostructure. Compared with 1L MoS_2/SiC, 2L MoS_2/SiC possess thicker layers, smaller bandgap distribution, and type II band alignment, which would more effectively improve the light absorption, separate the photogenerated carriers and enhance the performance of optoelectronic devices.

For 4L MoS_2/SiC interface, the interface states also locate at the region from Si2 to S2, and Fermi level is pinned at them, similar with the cases in the 1L and 2L MoS_2/SiC interfaces. Except the lowest MoS_2 monolayer, the upper MoS_2 layers show almost no interface states in the bandgap and the Fermi level just passes through the center of the bandgap. Therefore, Fermi level was just pinning at the interface states in the lowest 1L MoS_2/SiC heterostructure. The interaction between the upper MoS_2 layers and lowest MoS_2 monolayer keeps the weak vdW interaction, similar with the case of 2L MoS_2/SiC interface.

The evolution of CBM and VBM of 4L MoS_2/SiC interface, as indicated by the red dashed lines in Fig. 8(c), exhibits the similar trend as that of 2L MoS_2/SiC interface. Atomic DOSs of bottom C1, Si1 and C2 also exhibit the inner SiC electronic properties with the bandgap of about 3.23 eV. The CBM and VBM also lie at the –0.13 and –3.36 eV, respectively. Looking up from Si2 to S2, the CBM firstly shifts a little down to –0.37 eV. Then, the CBM shifts largely up to 0.48 eV from S3 to S6, indicating the weak vdW interaction between the upper and lowest MoS_2 layer. And from S7 to S8, the CBM shifts a little down to 0.19 eV. For the VBM, it firstly shifts largely up to –1.90 eV from C4 to S1. Then, the VBM continues to shift up to –1.00 eV from Mo1 to S6 due to the interlayer orbital coupling interaction in quadlayer MoS_2. Finally, the VBM shifts a little down to –1.29 eV. Then the bandgap changes from 3.23 eV to 2.99 eV, 1.53 eV, 0.63 eV, 1.48 eV, and 1.48 eV from bottom to up in the 4L MoS_2/SiC heterostructure. The CBM locates at the interface of lowest MoS_2 and SiC substrate from Si2 to S2, while the VBM locates at the MoS_2 layer from Mo1 to S6. The 4L MoS_2/SiC heterostructure also exhibits the type II band alignment. It will have similar advantages to 2L MoS_2/SiC in enhancing electronic and optoelectronic device performance.

Figures 9 (a)–(c) exhibits the theoretical energy band alignments at 1L, 2L, and 4L MoS_2/SiC interfaces. The 1L MoS_2/SiC interface exhibits the type I band alignment with the CBO of 0.20 eV and VBO of 1.46 eV. The large VBO and small CBO are attributed to the strong interaction between 1L MoS_2 and SiC substrate and the Fermi level pinning at the interface states. Due to the asymmetric CBM and VBM evolution, it is different from the traditional type I band alignment. Further due to the built-in electric field, the photogenerated electrons accumulate at SiC region, while the photogenerated holes accumulate at MoS_2 region.

For the 2L (4L) MoS_2/SiC interface, they exhibit the type II band alignments and the CBO and VBO are 0.80 (0.61) and 2.22 (2.36) eV, respectively. The enlarged CBOs and VBOs, as compared to that of 1L MoS_2/SiC, are attributed to the weak vdW interaction between the lower MoS_2 monolayer and upper MoS_2 layers and the strong interlayer orbital coupling. Then the photogenerated electrons and holes tend to accumulate to the SiC and MoS_2 layer, respectively, due to type II band alignment and built-in electric field. The high efficiency of charge separation in these heterostructures will enhance the device performance significantly. Finally, both the experimental and theoretical (2H-phase stacking) VBOs of the 1L, 2L and 4L MoS_2/SiC interfaces were ploted in Fig. 9(d). As the MoS_2 thickness increasing from 1L to 4L, the experimental VBO increases from 1.49 eV to 2.04 eV and 2.19 eV. Theoretically, the VBO (2H-phase stacking) increases from 1.46 eV to 2.22 eV and 2.36 eV. Therefore, the experimental and theoretical (2H-phase stacking) VBOs are in good agreement with each other, confirming the validity of the interface properties demonstrated in this study.

Since the metastable 3R-phase stacking MoS_2 were also observed in experiments, we further calculated the atomic DOSs of the 3R-phase stacking 2L and 4L MoS_2/

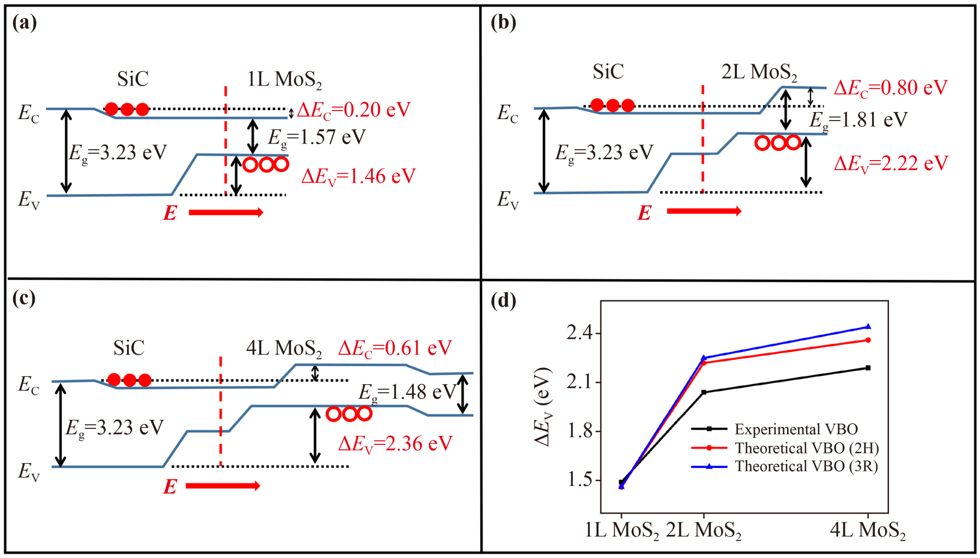

Fig. 9 Theoretical energy band alignments at **(a)** 1L, **(b)** 2L, and **(c)** 4L MoS_2/SiC interfaces. The red dashed line indicates the real space boundary between the SiC and MoS_2 layers. The VBO and CBO were indicated by ΔE_V and ΔE_C. The built-in electric field and photogenerated electrons and holes were denoted by the red arrow, red solid and hollow circles, respectively. **(d)** Comparison of the experimental and theoretical VBOs (2H-phase and 3R-phase stacking) of the 1L, 2L and 4L MoS_2/SiC interfaces.

SiC heterostructures and the theoretical VBOs (3R-phase stacking) of the 2L and 4L MoS_2/SiC interfaces were also exhibited in Fig. 9(d) for comparison. The VBOs of 3R-phase stacking structure increase from 1.46 eV to 2.25 eV and 2.44 eV. As compared to that of 2H-phase, the increased theoretical VBO of 3R-phase stacking is attributed to the small shrunken bandgap and enlarged VBM of the 3R-phase MoS_2, which is agreement with the previous study [71]. Therefore, both the theoretical 2H- and 3R-phase VBOs are in good agreement with each other, and the 2H- and 3R-phase stacking structures do not influence significantly the interfacial properties, especially the band alignment, of multilayer MoS_2/SiC heterostructures.

4 Conclusions

In summary, the interfacial properties of 2D/3D MoS_2/4H-SiC heterostructures were studied by XPS and first-principles calculations. It is found that the VBO increases from 1.49 eV to 2.19 eV with increasing MoS_2 layers up to 4L, consistent with the first-principles calculations. For 1L MoS_2/SiC, a strong interlayer interaction between the 1L MoS_2 and SiC sheet was demonstrated by the formation of a chemical Si-S bond (2.20 Å) and a large binding energy (–0.96 eV/unit cell). Then Fermi level pinning at the interface states and a passivation of 4H-SiC (0001) Si surface were realized. About 0.96e per unit cell transferring from SiC to MoS_2 monolayer indicates an electric field forms, and it directs from SiC to MoS_2. Then, the 1L MoS_2/SiC interface exhibits the type I band alignment with the CBO of 0.20 eV and VBO of 1.46 eV. The large VBO and small CBO are attributed to the strong interaction between 1L MoS_2 and SiC substrate and the Fermi level pinning at the interface states. For 2L and 4L MoS_2/SiC, Fermi level was just pinning at the lower MoS_2 monolayer. The interaction between the upper MoS_2 layers and lower MoS_2 monolayer keeps the weak vdW interaction. Then, they exhibit the type II band alignments and the CBO and VBO are 0.80 (0.61) and 2.22 (2.36) eV, respectively. The enlarged CBOs and VBOs are attributed to the weak vdW interaction between the lower MoS_2 monolayer and upper MoS_2 layers and the strong interlayer orbital coupling. Despite of the different band alignment type, the photogenerated electrons and holes tend to accumulate to the SiC and MoS_2 layer, respectively, due to the asymmetric band alignment and built-in electric field in all the 1L, 2L and 4L MoS_2/SiC interfaces. The high efficiency of charge separation in these heterostructures will enhance the device performance significantly. The multiple interfacial interactions discussed in this study provide a new modulated perspective for the next-generation electronics and optoelectronics based on the 2D/3D semiconductors heterojunctions.

Acknowledgements This work was supported by Fujian Minjiang Scholar Program, Fujian Hundred-Talent Program, the National Natural Science Foundation of China (Grant Nos. 11804115, 22172062 and 62171396), the Foundation from Department of Science and Technology of Fujian Province (Grant Nos. 2019L3008, 2020J01704, 2021J01863, 2021J05171, and 2022J01822), the Foundation from Department of Education of Fujian Province (Grant No. JT180261), and the Scientific Research Foundation from Jimei University (Grant Nos. ZC2018007, ZQ2019008, ZP2020066, and ZP2020065).

References

1. H. W. Kroto, J. R. Heath, S. C. O'Brien, R. F. Curl, and R. E. Smalley, C_{60}: Buckminsterfullerene, *Nature* 318(6042), 162 (1985)
2. D. S. Bethune, C. H. Kiang, M. S. de Vries, G. Gorman, R. Savoy, J. Vazquez, and R. Beyers, Cobalt-catalysed growth of carbon nanotubes with single-atomic-layer walls, *Nature* 363(6430), 605 (1993)
3. K. S. Novoselov, A. K. Geim, S. V. Morozov, D. Jiang, Y. Zhang, S. V. Dubonos, I. V. Grigorieva, and A. A. Firsov, Electric field effect in atomically thin carbon films, *Science* 306(5696), 666 (2004)
4. L. Song, L. Ci, H. Lu, P. B. Sorokin, C. Jin, J. Ni, A. G. Kvashnin, D. G. Kvashnin, J. Lou, B. I. Yakobson, and P. M. Ajayan, Large scale growth and characterization of atomic hexagonal boron nitride layers, *Nano Lett.* 10(8), 3209 (2010)
5. L. Li, Y. Yu, G. J. Ye, Q. Ge, X. Ou, H. Wu, D. Feng, X. H. Chen, and Y. Zhang, Black phosphorus field-effect transistors, *Nat. Nanotechnol.* 9(5), 372 (2014)
6. P. J. Wang, D. Y. Yang, and X. D. Pi, Toward wafer-scale production of 2D transition metal chalcogenides, *Adv. Electron. Mater.* 7(8), 2100278 (2021)
7. M. J. Allen, V. C. Tung, and R. B. Kaner, Honeycomb carbon: A review of graphene, *Chem. Rev.* 110(1), 132 (2010)
8. S. Imani Yengejeh, W. Wen, and Y. Wang, Mechanical properties of lateral transition metal dichalcogenide heterostructures, *Front. Phys.* 16(1), 13502 (2021)
9. R. Szczęśniak, A. P. Durajski, and M. W. Jarosik, Strong-coupling superconductivity induced by calcium intercalation in bilayer transition-metal dichalcogenides, *Front. Phys.* 13(2), 137401 (2018)
10. Y. P. Venkata Subbaiah, K. J. Saji, and A. Tiwari, Atomically thin MoS_2: A versatile nongraphene 2D material, *Adv. Funct. Mater.* 26(13), 2046 (2016)
11. S. A. Han, R. Bhatia, and S. W. Kim, Synthesis, properties and potential applications of two-dimensional transition metal dichalcogenides, *Nano Converg.* 2, 17 (2015)
12. H. L. Zhu, C. J. Zhou, X. J. Huang, X. L. Wang, H. Z. Xu, Y. Lin, W. H. Yang, Y. P. Wu, W. Lin, and F. Guo, Evolution of band structures in MoS_2-based homo- and heterobilayers, *J. Phys. D* 49(6), 065304 (2016)
13. B. Radisavljevic, A. Radenovic, J. Brivio, V. Giacometti, and A. Kis, Single-layer MoS_2 transistors, *Nat. Nanotechnol.* 6(3), 147 (2011)
14. Y. D. Zhao, K. Xu, F. Pan, C. J. Zhou, F. C. Zhou, and Y. Chai, Doping, contact and interface engineering of two-dimensional layered transition metal dichalcogenides transistors, *Adv. Funct. Mater.* 27(19), 1603484 (2017)
15. L. Teitz and M. C. Toroker, Theoretical investigation of dielectric materials for two-dimensional field-effect transistors, *Adv. Funct. Mater.* 30(18), 1808544 (2020)
16. E. Z. Zhang, W. Y. Wang, C. Zhang, Y. B. Jin, G. D. Zhu, Q. Q. Sun, D. W. Zhang, P. Zhou, and F. X. Xiu, Tunable charge-trap memory based on few-layer MoS_2, *ACS Nano* 9(1), 612 (2015)
17. N. Li, Q. Q. Wang, C. Shen, Z. Wei, H. Yu, J. Zhao, X. B. Lu, G. L. Wang, C. L. He, L. Xie, J. Q. Zhu, L. J. Du, R. Yang, D. X. Shi, and G. Y. Zhang, Large-scale flexible and transparent electronics based on monolayer molybdenum disulfide field-effect transistors, *Nat. Electron.* 3(11), 711 (2020)
18. M. Y. Tsai, A. Tarasov, Z. R. Hesabi, H. Taghinejad, P. M. Campbell, C. A. Joiner, A. Adibi, and E. M. Vogel, Flexible MoS_2 field-effect transistors for gate-tunable piezoresistive strain sensors, *ACS Appl. Mater. Interfaces* 7(23), 12850 (2015)
19. J. M. Choi, H. Y. Jang, A. R. Kim, J. D. Kwon, B. Cho, M. H. Park, and Y. Kim, Ultraflexible and rollable 2D-MoS_2/Si heterojunction-based near-infrared photodetector via direct synthesis, *Nanoscale* 13(2), 672 (2021)
20. Y. F. Xiao, L. Min, X. K. Liu, W. J. Liu, U. Younis, T. H. Peng, X. W. Kang, X. H. Wu, S. J. Ding, and D. W. Zhang, Facile integration of MoS_2/SiC photodetector by direct chemical vapor deposition, *Nanophotonics* 9(9), 3035 (2020)
21. K. Zhang, M. Z. Peng, A. F. Yu, Y. J. Fan, J. Y. Zhai, and Z. L. Wang, A substrate-enhanced MoS_2 photodetector through a dual-photogating effect, *Mater. Horiz.* 6(4), 826 (2019)
22. W. Z. Wang, X. B. Zeng, J. H. Warner, Z. Y. Guo, Y. S. Hu, Y. Zeng, J. J. Lu, W. Jin, S. B. Wang, J. C. Lu, Y. R. Zeng, and Y. H. Xiao, Photoresponse-bias modulation of a highperformance MoS_2 photodetector with a unique vertically stacked 2H-MoS_2/1T@2H-MoS_2 structure, *ACS Appl. Mater. Interfaces* 12(29), 33325 (2020)
23. M. X. Sun, P. F. Yang, D. Xie, Y. L. Sun, J. L. Xu, T. L. Ren, and Y. F. Zhang, Self-powered MoS_2-PDPP3T heterotransistor-based broadband photodetectors, *Adv. Electron. Mater.* 5(2), 1800580 (2019)
24. U. Krishnan, M. Kaur, K. Singh, M. Kumar, and A. Kumar, A synoptic review of MoS_2: Synthesis to applications, *Superlattices Microstruct.* 128, 274 (2019)
25. Y. Liu, Y. J. Fang, D. R. Yang, X. D. Pi, and P. J. Wang, Recent progress of heterostructures based on two dimensional materials and wide bandgap semiconductors, *J. Phys.: Condens. Matter* 34(18), 183001 (2022)
26. C. Langpoklakpam, A. C. Liu, K. H. Chu, L. H. Hsu, W. C. Lee, S. C. Chen, C. W. Sun, M. H. Shih, K. Y. Lee, and H. C. Kuo, Review of silicon carbide processing for power MOSFET, *Crystals (Basel)* 12(2), 245 (2022)
27. F. Roccaforte, P. Fiorenza, M. Vivona, G. Greco, and F. Giannazzo, Selective doping in silicon carbide power devices, *Materials (Basel)* 14(14), 3923 (2021)
28. M. S. Kang, C. H. Lee, J. B. Park, H. Yoo, and G. C. Yi, Gallium nitride nanostructures for light-emitting diode applications, *Nano Energy* 1(3), 391 (2012)
29. Y. Sun, X. W. Kang, Y. K. Zheng, J. Lu, X. L. Tian, K. Wei, H. Wu, W. B. Wang, X. Y. Liu, and G. Q. Zhang, Review of the recent progress on GaN-based vertical power Schottky barrier diodes (SBDs), *Electronics (Basel)* 8(5), 575 (2019)
30. N. G. Wright, A. B. Horsfall, and K. Vassilevski, Prospects for SiC electronics and sensors, *Mater. Today* 11(1–2), 16 (2008)
31. N. Goel, R. Kumar, B. Roul, M. Kumar, and S. B. Krupanidhi, Wafer-scale synthesis of a uniform film of few-layer MoS_2 on GaN for 2D heterojunction ultraviolet photodetector, *J. Phys. D* 51(37), 374003 (2018)

32. M. Moun, M. Kumar, M. Garg, R. Pathak, and R. Singh, Understanding of MoS_2/GaN heterojunction diode and its photodetection properties, *Sci. Rep.* 8, 11799 (2018)
33. A. Aldalbahi, E. Li, M. Rivera, R. Velazquez, T. Altalhi, X. Y. Peng, and P. X. Feng, A new approach for fabrications of SiC based photodetectors, *Sci. Rep.* 6, 23457 (2016)
34. W. Gao, F. Zhang, Z. Q. Zheng, and J. B. Li, Unique and tunable photodetecting performance for two-dimensional layered $MoSe_2$/WSe_2 p–n junction on the 4H-SiC substrate, *ACS Appl. Mater. Interfaces* 11(21), 19277 (2019)
35. Z. Cui, K. F. Bai, Y. C. Ding, X. Wang, E. L. Li, and J. S. Zheng, Janus XSSe/SiC (X = Mo, W) van der Waals heterostructures as promising water-splitting photocatalysts, *Physica E* 123, 114207 (2020)
36. M. A. Hassan, M. W. Kim, M. A. Johar, A. Waseem, M. K. Kwon, and S. W. Ryu, Transferred monolayer MoS_2 onto GaN for heterostructure photoanode: Toward stable and efficient photoelectrochemical water splitting, *Sci. Rep.* 9, 20141 (2019)
37. N. Goel, R. Kumar, S. K. Jain, S. Rajamani, B. Roul, G. Gupta, M. Kumar, and S. B. Krupanidhi, A high-performance hydrogen sensor based on a reverse-biased MoS_2/GaN heterojunction, *Nanotechnology* 30(31), 314001 (2019)
38. M. Reddeppa, B. G. Park, G. Murali, S. H. Choi, N. D. Chinh, D. Kim, W. Yang, and M. D. Kim, NO_x gas sensors based on layer-transferred n-MoS_2/p-GaN heterojunction at room temperature: Study of UV light illuminations and humidity, *Sens. Actuators B Chem.* 308, 127700 (2020)
39. Y. H. Ji, A. P. Huang, M. Q. Yang, Q. Gao, X. L. Yang, X. L. Chen, M. Wang, Z. S. Xiao, R. Z. Wang, and P. K. Chu, Wrinkled-surface-induced memristive behavior of MoS_2 wrapped GaN nanowires, *Adv. Electron. Mater.* 6(10), 2000571 (2020)
40. G. Kresse and J. Hafner, *Ab initio* molecular dynamics for liquid metals, *Phys. Rev. B* 47(1), 558 (1993)
41. J. P. Perdew, K. Burke, and M. Ernzerhof, Generalized gradient approximation made simple, *Phys. Rev. Lett.* 77(18), 3865 (1996)
42. S. Grimme, J. Antony, S. Ehrlich, and H. Krieg, A consistent and accurate ab initio parametrization of density functional dispersion correction (DFT-D) for the 94 elements H-Pu, *J. Chem. Phys.* 132(15), 154104 (2010)
43. J. Heyd, G. E. Scuseria, and M. Ernzerhof, Hybrid functionals based on a screened Coulomb potential, *J. Chem. Phys.* 118(18), 8207 (2003)
44. L. Bengtsson, Dipole correction for surface supercell calculations, *Phys. Rev. B* 59(19), 12301 (1999)
45. G. Henkelman, A. Arnaldsson, and H. Jonsson, A fast and robust algorithm for Bader decomposition of charge density, *Comput. Mater. Sci.* 36(3), 354 (2006)
46. J. G. Tao, J. W. Chai, Z. Zhang, J. S. Pan, and S. J. Wang, The energy-band alignment at molybdenum disulphide and high-k dielectrics interfaces, *Appl. Phys. Lett.* 104(23), 232110 (2014)
47. J. G. Tao, J. W. Chai, X. Lu, L. M. Wong, T. I. Wong, J. S. Pan, Q. H. Xiong, D. Z. Chi, and S. J. Wang, Growth of wafer-scale MoS_2 monolayer by magnetron sputtering, *Nanoscale* 7(6), 2497 (2015)
48. W. F. Yang, H. Kawai, M. Bosman, B. S. Tang, J. W. Chai, W. L. Tay, J. Yang, H. L. Seng, H. L. Zhu, H. Gong, H. F. Liu, K. E. J. Goh, S. J. Wang, and D. Z. Chi, Interlayer interactions in 2D WS_2/MoS_2 heterostructures monolithically grown by *in situ* physical vapor deposition, *Nanoscale* 10(48), 22927 (2018)
49. B. S. Tang, Z. G. Yu, L. Huang, J. W. Chai, S. L. Wong, J. Deng, W. F. Yang, H. Gong, S. J. Wang, K. W. Ang, Y. W. Zhang, and D. Z. Chi, Direct n- to p-type channel conversion in monolayer/few-layer WS_2 field-effect transistors by atomic nitrogen treatment, *ACS Nano* 12(3), 2506 (2018)
50. L. Cheng, X. B. Wang, W. F. Yang, J. W. Chai, M. Yang, M. J. Chen, Y. Wu, X. X. Chen, D. Z. Chi, K. E. J. Goh, J. X. Zhu, H. D. Sun, S. J. Wang, J. C. W. Song, M. Battiato, H. Yang, and E. E. M. Chia, Far out-of-equilibrium spin populations trigger giant spin injection into atomically thin MoS_2, *Nat. Phys.* 15(4), 347 (2019)
51. H. Li, Q. Zhang, C. C. R. Yap, B. K. Tay, T. H. T. Edwin, A. Olivier, and D. Baillargeat, From bulk to monolayer MoS_2: Evolution of Raman scattering, *Adv. Funct. Mater.* 22(7), 1385 (2012)
52. C. Lee, H. Yan, L. E. Brus, T. F. Heinz, J. Hone, and S. Ryu, Anomalous lattice vibrations of single- and few-layer MoS_2, *ACS Nano* 4(5), 2695 (2010)
53. B. Chakraborty, H. S. S. R. Matte, A. K. Sood, and C. N. R. Rao, Layer-dependent resonant Raman scattering of a few layer MoS_2, *J. Raman Spectrosc.* 44(1), 92 (2013)
54. H. Deng, K. Endo, and K. Yamamura, Competition between surface modification and abrasive polishing: A method of controlling the surface atomic structure of 4H-SiC (0001), *Sci. Rep.* 5, 8947 (2015)
55. Q. Wang, X. H. Cheng, L. Zheng, P. Y. Ye, M. L. Li, L. Y. Shen, J. J. Li, D. L. Zhang, Z. Y. Gu, and Y. H. Yu, Interfacial chemistry and energy band alignment of TiAlO on 4H-SiC determined by X-ray photoelectron spectroscopy, *Appl. Surf. Sci.* 409, 71 (2017)
56. N. M. D. Brown, N. Y. Cui, and A. McKinley, An XPS study of the surface modification of natural MoS_2 following treatment in an RF-oxygen plasma, *Appl. Surf. Sci.* 134(1–4), 11 (1998)
57. G. Eda, H. Yamaguchi, D. Voiry, T. Fujita, M. W. Chen, and M. Chhowalla, Photoluminescence from chemically exfoliated MoS_2, *Nano Lett.* 11(12), 5111 (2011)
58. M. A. Baker, R. Gilmore, C. Lenardi, and W. Gissler, XPS investigation of preferential sputtering of S from MoS_2 and determination of MoS_x stoichiometry from Mo and S peak positions, *Appl. Surf. Sci.* 150(1–4), 255 (1999)
59. L. X. Cheng, X. Y. Qin, A. T. Lucero, A. Azcatl, J. Huang, R. M. Wallace, K. Cho, and J. Kim, Atomic layer deposition of a high-k dielectric on MoS_2 using trimethylaluminum and ozone, *ACS Appl. Mater. Interfaces* 6(15), 11834 (2014)
60. A. Santoni, F. Biccari, C. Malerba, M. Valentini, R.

Chierchia, and A. Mittiga, Valence band offset at the CdS/Cu_2ZnSnS_4 interface probed by X-ray photoelectron spectroscopy, *J. Phys. D* 46(17), 175101 (2013)

61. H. M. Hill, A. F. Rigosi, K. T. Rim, G. W. Flynn, and T. F. Heinz, Band alignment in MoS_2/WS_2 transition metal dichalcogenide heterostructures probed by scanning tunneling microscopy and spectroscopy, *Nano Lett.* 16(8), 4831 (2016)
62. L. Lin, Y. J. Chen, L. W. Yao, J. T. Huang, R. X. Chen, X. Chen, and H. L. Tao, First-principles study of In and Mn dopants on the magnetic and optical properties of 4H-SiC, *J. Lumin.* 239, 118341 (2021)
63. A. Bauer, J. Krausslich, L. Dressler, P. Kuschnerus, J. Wolf, K. Goetz, P. Kackell, J. Furthmuller, and F. Bechstedt, High-precision determination of atomic positions in crystals: The case of 6H- and 4H-SiC, *Phys. Rev. B* 57(5), 2647 (1998)
64. Y. X. Chen, X. Xu, P. Y. Liu, W. G. Xie, K. Chen, L. L. Shui, C. Q. Shang, Z. H. Chen, X. G. Ma, G. F. Zhou, T. T. Shi, and X. Wang, Unusual mechanism behind enhanced photocatalytic activity and surface passivation of SiC(0001) via forming heterostructure with a MoS_2 monolayer, *J. Phys. Chem. C* 124(2), 1362 (2020)
65. C. Gong, L. Colombo, R. M. Wallace, and K. Cho, The unusual mechanism of partial Fermi level pinning at metal-MoS_2 interfaces, *Nano Lett.* 14(4), 1714 (2014)
66. Z. F. Zhang, Q. K. Qian, B. K. Li, and K. J. Chen, Interface engineering of monolayer MoS_2/GaN hybrid heterostructure: Modified band alignment for photocatalytic water splitting application by nitridation treatment, *ACS Appl. Mater. Interfaces* 10(20), 17419 (2018)
67. H. L. Zhu, C. J. Zhou, X. L. Wang, X. W. Chen, W. H. Yang, Y. P. Wu, and W. Lin, Doping behaviors of adatoms adsorbed on phosphorene, *Phys. Status Solidi B* 253(6), 1156 (2016)
68. H. L. Zhu, C. J. Zhou, B. S. Tang, W. F. Yang, J. W. Chai, W. L. Tay, H. Gong, J. S. Pan, W. D. Zou, S. J. Wang, and D. Z. Chi, Band alignment of 2D WS_2/HfO_2 interfaces from X-ray photoelectron spectroscopy and first-principles calculations, *Appl. Phys. Lett.* 112(17), 171604 (2018)
69. M. Yang, J. W. Chai, M. Callsen, J. Zhou, T. Yang, T. T. Song, J. S. Pan, D. Z. Chi, Y. P. Feng, and S. J. Wang, Interfacial interaction between HfO_2 and MoS_2: From thin films to monolayer, *J. Phys. Chem. C* 120(18), 9804 (2016)
70. C. J. Zhou, H. L. Zhu, W. F. Yang, Q. B. Lin, T. C. Zheng, L. Yang, and S. Q. Lan, Interfacial properties of 2D WS_2 on SiO_2 substrate from X-ray photoelectron spectroscopy and first-principles calculations, *Front. Phys.* 17(5), 53500 (2022)
71. T. Cusati, A. Fortunelli, G. Fiori, and G. Iannaccone, Stacking and interlayer electron transport in MoS_2, *Phys. Rev. B* 98(11), 115403 (2018)